

Observation of the 4π -periodic Josephson effect in InAs nanowires

Dominique Laroche,^{1,*} Daniël Bouman,^{1,*} David J. van Woerkom,¹ Alex Proutski,¹
Chaitanya Murthy,² Dmitry I. Pikulin,³ Chetan Nayak,^{2,3} Ruben J. J. van Gulik,¹
Jesper Nygård,⁴ Peter Krogstrup,⁴ Leo P. Kouwenhoven,^{1,5} and Attila Geresdi^{1,†}

¹*QuTech and Kavli Institute of Nanoscience, Delft University of Technology, 2600 GA Delft, The Netherlands*

²*Department of Physics, University of California, Santa Barbara, CA 93106, USA*

³*Station Q, Microsoft Research, Santa Barbara, California 93106-6105, USA*

⁴*Center for Quantum Devices and Station Q Copenhagen, Niels Bohr Institute, University of Copenhagen, Universitetsparken 5, 2100 Copenhagen, Denmark*

⁵*Microsoft Station Q Delft, 2600 GA Delft, The Netherlands*

(Dated: September 2, 2022)

Quantum computation by non-Abelian Majorana zero modes (MZMs) [1, 2] offers an approach to achieve fault tolerance by encoding quantum information in the non-local charge parity states of semiconductor nanowire networks in the topological superconductor regime [3–5]. Thus far, experimental studies of MZMs chiefly relied on single electron tunneling measurements [6–11] which leads to decoherence of the quantum information stored in the MZM [4, 12]. As a next step towards topological quantum computation, charge parity conserving experiments based on the Josephson effect [13] are required, which can also help exclude suggested non-topological origins [14–18] of the zero bias conductance anomaly. Here we report the direct measurement of the Josephson radiation frequency [19] in InAs nanowires with epitaxial aluminium shells [20]. For the first time, we observe the 4π -periodic Josephson effect above a magnetic field of ≈ 200 mT, consistent with the estimated [21, 22] and measured [23] topological phase transition of similar devices.

The universal relation between the frequency f_J of the oscillating current and an applied DC voltage bias V across a superconducting weak link [13] is determined solely by natural constants:

$$\frac{f_J}{V} = \frac{2e}{h} = \Phi_0^{-1} = 483.6 \text{ MHz}/\mu\text{V}, \quad (1)$$

where e is the single electron charge, h is the Planck constant and Φ_0 is the superconducting flux quantum. This relation, describing the conventional, 2π -periodic Josephson effect, can be understood as the tunneling of Cooper pairs with a net charge $e^* = 2e$ coupled to photons of energy hf [24]. This coupling, referred to as the AC Josephson effect, has first been measured in superconducting tunnel junctions [25] and has been shown to persist in metallic weak links [26], carbon nanotubes [27] and semiconductor channels [28, 29], as well as in high critical temperature superconductors [30].

In topological Josephson junctions, the effective tunneling charge is the single electron charge, $e^* = e$, which

leads to a factor of two increase in the flux periodicity, giving rise to the so-called 4π -periodic Josephson effect [21, 22, 31]. Therefore, in this MZM regime, the frequency at a given voltage bias V drops by a factor of two, $f_{\text{MZM}}(V) = f_J(V)/2$, providing a robust signature of the topological phase transition in the superconducting leads. In real devices however, the finite size of the topological regions [32], poisoning events [22, 31] and Landau-Zener tunneling to the quasiparticle continuum [33] can effectively restore the 2π -periodic, trivial state. The latter two parity-mixing effects cause the system to relax to its ground state, effectively constraining the system in the lowest topological energy branch (red solid lines in Fig. 1a). Nevertheless, out-of-equilibrium measurements performed at rates faster than these equilibration processes can still capture the 4π -periodic nature of topological junctions [32–34]. In contrast, finite-size effects can be avoided by biasing the junction at voltages large enough to overcome the Majorana hybridization gap ε_M [33].

Here, we report the direct observation of a magnetic field-induced halving of the Josephson radiation frequency in InAs nanowire (NW) junctions partially covered with an epitaxially grown aluminium shell [20] (Fig. 1d). In this system, previous direct transport experiments suggest parity lifetimes above $0.1 \mu\text{s}$ [35] and hybridization energies $\varepsilon_M \lesssim 1 \mu\text{eV}$ for leads longer than $1.5 \mu\text{m}$ [36]. Thus, a frequency-sensitive measurement in the microwave domain is expected to reveal the 4π -periodic Josephson effect [37, 38].

As a frequency-sensitive microwave detector, we utilize a superconducting tunnel junction with a quasiparticle gap of Δ_{DET} , wherein the photon-assisted electron tunneling (PAT) current contributes to the DC current above a voltage bias threshold $eV_{\text{DET}} > 2\Delta_{\text{DET}} - hf$ [19, 39] (Fig. 1c). This *on-chip* detector [40], coupled via capacitors C_C to the NW junction (see Fig. 1b for the schematics and Fig. 1e for optical image of the device) is engineered to result in an overdamped microwave environment characterized by a single $f_c = (2\pi RC)^{-1} \approx 28 \text{ GHz}$ cutoff frequency with $R = 538 \Omega$ and $C = 10.4 \text{ fF}$, see Sec. 3 in the Supplementary Information (SI). The re-

sulting broadband coupling to the detector [29] inhibits higher order photon emission, which could mimic the 4π -periodic Josephson effect [41].

The nanowire is deterministically deposited on a set of three gates covered by 30 nm thick SiN_x dielectric as shown in Fig. 1d. The Josephson weak link, where the Al shell is removed by wet chemical etching, is located above the central gate (see inset of Fig. 1d). We investigated devices with junction lengths ranging from 86 nm to 271 nm. The high quality of the nanowire junction is apparent from the presence of distinct multiple Andreev reflection steps in its $I_{\text{NW}}(V_{\text{NW}})$ characteristics [42] (Fig. 1g).

The microwave detector, presented in Fig. 1f, is fabricated using two angle-evaporated [43] Al/ AlO_x /Al tunnel junctions, forming a superconducting quantum interference device (SQUID). This geometry allows us to minimize the Josephson energy of the detector by applying $\Phi = \Phi_0/2$ flux through the loop (see Fig. 1h) and thus to limit its backaction to the nanowire. The respectively 8 and 11 nm thick Al layers set an *in-plane* critical magnetic field of the detector in excess of 1 T, well above the measured topological transition in similar devices [23]. The circuit parameters and fabrication details are given in Sec. 1 of the SI.

In the presence of a voltage spectral density $S_V(f)$, the DC current contribution of the PAT process is as follows [19, 39] in the subgap regime, where $eV_{\text{DET}} < 2\Delta_{\text{DET}}$:

$$I_{\text{PAT}}(V_{\text{DET}}) = \int_0^\infty df \left(\frac{e}{hf} \right)^2 S_V(f) I_{\text{QP},0} \left(V_{\text{DET}} + \frac{hf}{e} \right). \quad (2)$$

Here, $I_{\text{QP},0}(eV_{\text{DET}})$ is the tunnel junction current in the absence of absorbed radiation, $S_V(f) = 0$ (see Fig. 1h). Note that the quasiparticle gap edge at $eV_{\text{DET}} = 2\Delta_{\text{DET}}$ results in a sharp increase of $I_{\text{QP},0}(eV_{\text{DET}})$. In the presence of monochromatic radiation with a frequency f_0 , $S_V(f) \sim \delta(f - f_0)$, I_{PAT} thus develops a step-like feature at $hf_0 = 2\Delta_{\text{DET}} - eV_{\text{DET}}$. With a phenomenological effective charge e^* of the AC Josephson effect, we write this condition in terms of the voltage drop on the nanowire, V_{NW} :

$$e^*V_{\text{NW}} = hf_0 = 2\Delta_{\text{DET}} - eV_{\text{DET}}, \quad (3)$$

where $e^* = 2e$ for conventional junctions (see Eq. (1)) and $e^* = e$ in the 4π -periodic regime. To extract e^* and thus determine the periodicity of the Josephson radiation, we track the transconductance peak $dI_{\text{PAT}}/dV_{\text{NW}}(V_{\text{NW}}, V_{\text{DET}})$ measured by standard lock-in techniques at a frequency of 17.7 Hz. The experiments were performed at the base temperature of a dilution refrigerator (~ 20 mK).

Typical experimental datasets are shown in Fig. 2 for two nanowire junctions (NW1 and NW2, respectively), and one Al/ AlO_x /Al tunnel junction (T) as the source of Josephson radiation. We limit the detector voltage

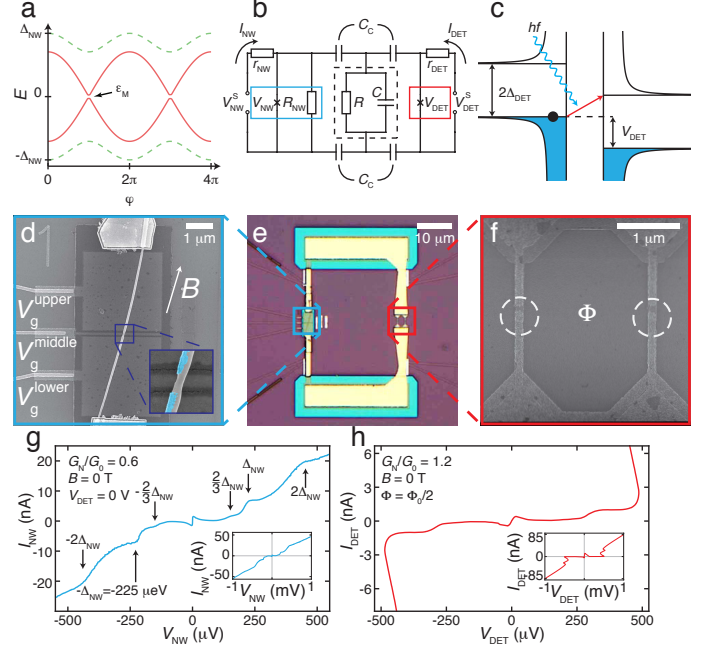


FIG. 1. Principles of the experiment. (a) Energy dispersion of topologically trivial (dashed green line) and nontrivial (solid red line) Andreev levels inside a NW Josephson junction as a function of the phase difference across the junction. The gap ϵ_M arises from the finite MZMs wavefunction overlap. (b) Equivalent circuit diagram of the device. The NW junction (in blue box) is capacitively coupled to the superconducting tunnel junction (red box) via the capacitors C_C . The microwave losses and stray capacitance are modeled by the RC element enclosed by the dashed black box, see text. The applied DC bias voltages are V_{NW}^S and V_{DET}^S with an effective internal resistance r_{NW} and r_{DET} , respectively. (c) Principle of the frequency sensitive detection based on photon-assisted tunneling: an absorbed photon with an energy hf gives rise to quasiparticle current if $hf > 2\Delta_{\text{DET}} - eV_{\text{DET}}$. (d) Scanning electron micrograph of the NW junction placed on three electrostatic gates. A false color micrograph of the junction is shown in the inset, with the epitaxial Al shell highlighted in cyan. (e) Bright field optical image of the coupling circuitry between the NW junction (blue box) and the detector junction (red box). (f) Micrograph of the split tunnel junction detector. The junctions are encircled. (g) Measured $I_{\text{NW}}(V_{\text{NW}})$ characteristics of the NW junction at zero in-plane magnetic field exhibiting a supercurrent branch and multiple Andreev reflections. (h) Measured $I_{\text{DET}}(V_{\text{DET}})$ trace of the detector split junction at zero in-plane magnetic field with a minimized switching current. The insets in panels (g) and (h) show the large scale $I(V)$ trace of each junction. The normal state conductance, G_N is given in the units of $G_0 = 2e^2/h$. All images and data were taken on device NW1.

range by the condition $dI_{\text{DET}}/dV_{\text{DET}} < 10 \mu\text{S}$ where the subgap quasiparticle current is still negligible, typically $I_{\text{DET}} \lesssim 1$ nA. A lower limit of the emitter junction voltage is defined by the phase diffusion regime [44], characterized by periodic switching and retrapping events,

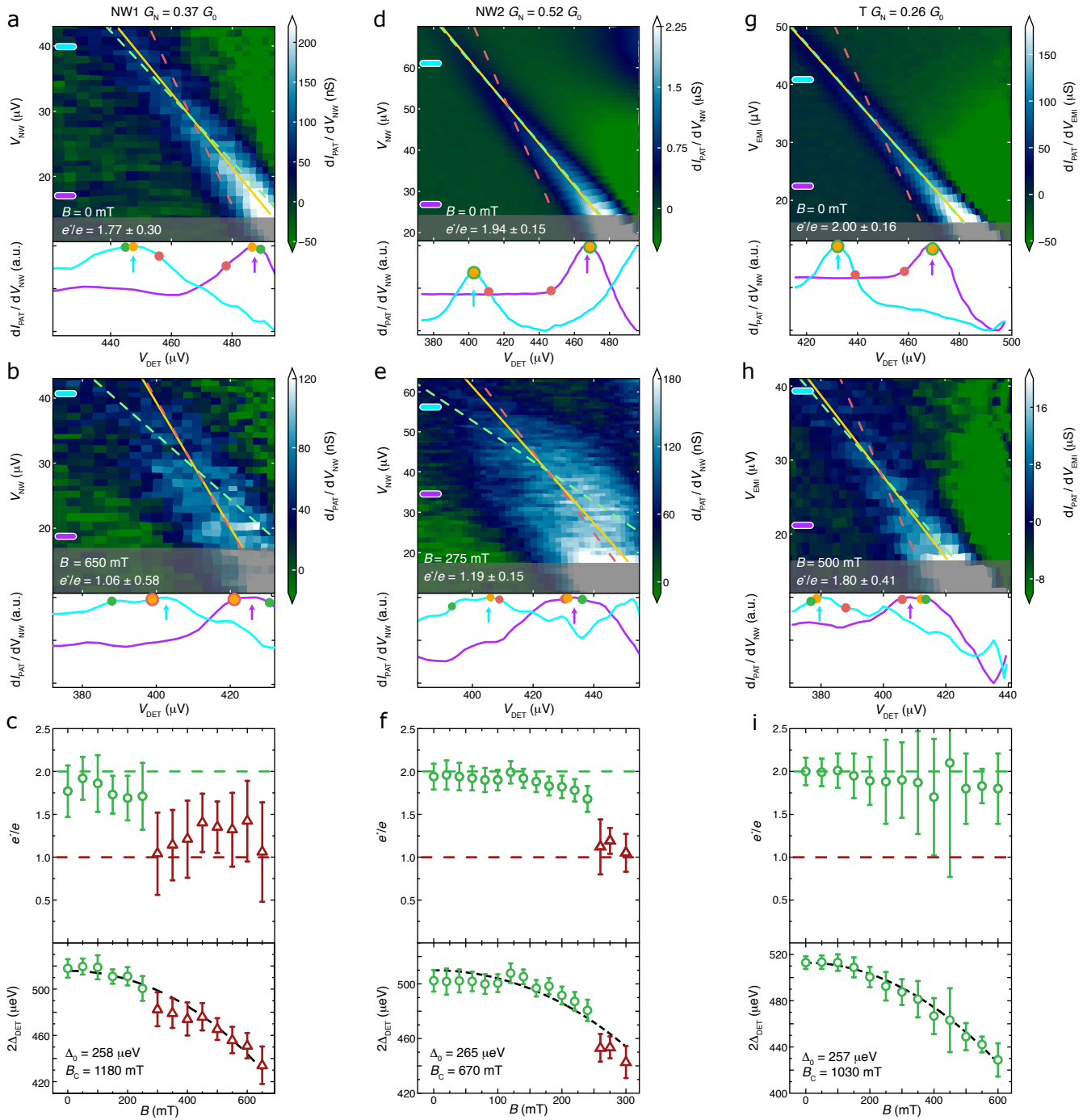


FIG. 2. **Magnetic field-induced 4π -periodic Josephson radiation.** Differential transconductance $dI_{\text{PAT}}/dV_{\text{NW}}$ as a function of V_{NW} and V_{DET} for device NW1 (panels (a) and (b)), NW2 (panels (d) and (e)) and T, an Al/AlO_x/Al tunnel junction (panels (g) and (h)) at zero and finite magnetic fields, respectively. The position of the transconductance peak maps the frequency of the monochromatic Josephson radiation. A linear fit $e^*V_{\text{NW}} = 2\Delta_{\text{DET}} - eV_{\text{DET}}$ through these peaks is shown as an orange line. Dashed green and red lines show linear fits with a fixed slope corresponding to $e^* = 2e$ and $e^* = e$, respectively. The shaded regions show the regimes where the fit of the transconductance peak is not reliable, see text. Two normalized and smoothed horizontal linecuts are plotted, where arrows point at the position of the extracted peaks. The orange, green and red dots denote the position of the best fit, the $e^* = 2e$ fit and the $e^* = e$ fit, respectively. The evolution of $e^*(B)$ and $2\Delta_{\text{DET}}(B)$ are presented in panels (c), (f) and (i). The transition from to 2π - to 4π -periodic Josephson radiation is observed between 175 and 300 mT for the NW devices as e^* evolves from values near $2e$ (green circles) to values close to e (red triangles). No such transition is observed for device T. For all devices, $2\Delta_{\text{DET}}(B)$ drops monotonically (black dashed line, see text), independently of the change in e^* .

which breaks the validity of Eq. (1) (see Fig. S16 in the SI). We therefore do not consider the low V_{NW} regime, within the supercurrent peak. We show this range, excluded from the linear fits, shaded in grey in Fig. 2 and Fig. 3 (see Fig. S5 in the SI on the characterization of these limits). We fit the peak positions using Eq. (3) in order to extract e^* and Δ_{DET} as a function of the applied in-plane magnetic field. The standard deviation of the fitted parameters is determined using the bootstrapping method [45]. For details, see Sec. 5 in the SI.

At zero magnetic field (Fig. 2a, d and g), the emitted Josephson radiation is always 2π -periodic with an extracted effective charge close to $e^* = 2e$, as shown by the good agreement between the orange line and the dashed green line (best fit with fixed $e^* = 2e$). In contrast, NW1 and NW2 exhibit the 4π -periodic Josephson effect above a threshold magnetic field (Fig. 2b and e), where $e^* \approx e$. The full evolution is shown in Fig. 2c and 2f, respectively, where a sharp transition is visible from $e^* \approx 2e$ (green circles) to $e^* \approx e$ (red triangles). However, the tunnel junction, where no topological phase transition is expected, exhibits $e^* \approx 2e$ in the same magnetic field range (Fig. 2h). Finally, the fitted Δ_{DET} (Fig. 2c, f and i) shows a monotonic decrease described by $2\Delta_{\text{DET}}(B) = 2\Delta_0\sqrt{1 - B^2/B_c^2}$ for all devices (dashed lines), with no additional feature at the transition field.

Fig. 3 shows the magnetic field evolution of device NW3 at two distinct gate settings. By tuning the chemical potential in the nanowire via changing the gate voltages, it is possible to displace the position of the onset of the 4π -periodic Josephson radiation from ≈ 175 mT (Fig. 3c) to values larger than 375 mT (Fig. 3f). Note that the additional local maximum at high V_{NW} values, also observed in earlier experiments [29], is attributed to the shot noise of the nanowire junction.

The possibility to tune the nanowire devices into the 4π -periodic Josephson radiation regime with both magnetic field and chemical potential is consistent with the predicted phase diagram of this system [21, 22, 31]. We observe the same behaviour in four distinct nanowire devices (see Fig. S7 in the SI for NW4), which we can interpret within the single subband model of the topological phase transition that takes place at a magnetic field B^* , where $E_z = g\mu_B B^*/2 = \sqrt{\Delta_{\text{NW}}^2 + \mu_{\text{NW}}^2}$. Here g and μ_B are the Landé g-factor and the Bohr magnetron, respectively. From our device parameters (see table S2 in the SI), lower bounds on the g-factors ranging from $g \approx 11$ ($B^* = 175$ mT) in device NW3 to $g \approx 35$ ($B^* = 190$ mT) in device NW4 are obtained, in agreement with values reported in similar devices [10, 23, 46]. In contrast, an accidental crossing of a trivial Andreev bound state would be inconsistent with the observed field range of $\Delta B \sim 0.3$ T of the 4π -periodic radiation, since within this range, a spinful Andreev level [46] would evolve over the scale of the superconducting gap, $\Delta_{\text{NW}} \sim g\mu_B \Delta B$ suppressing the 4π periodicity.

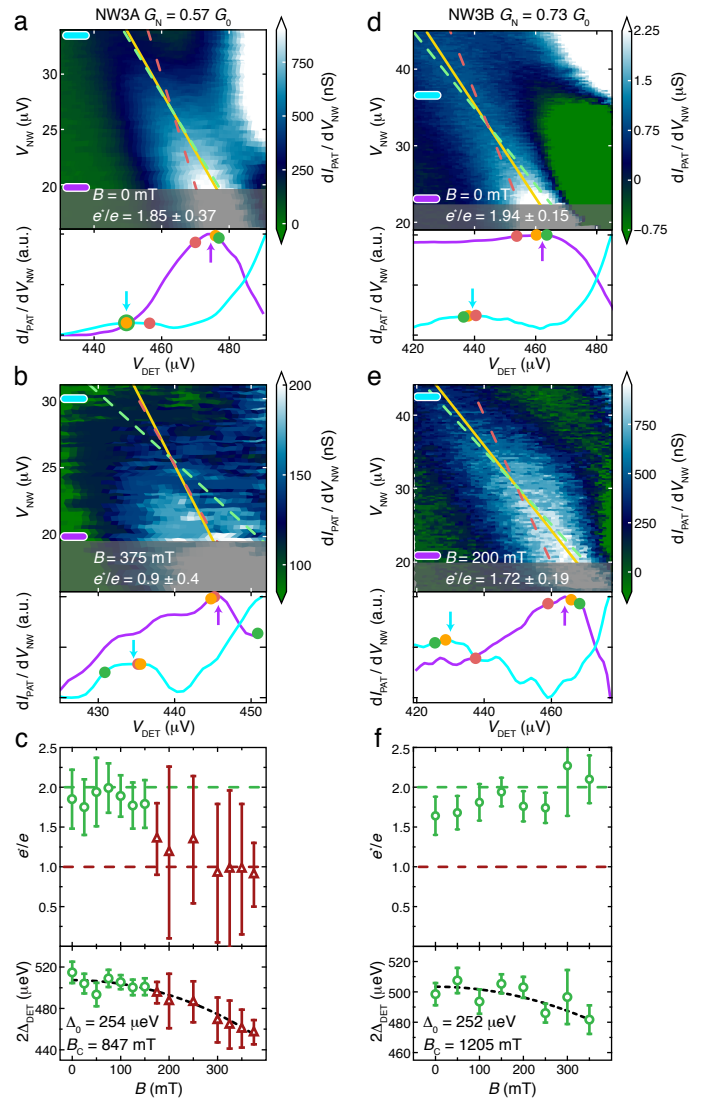


FIG. 3. Gate tuning of the 4π -periodic radiation regime. Differential transconductance $dI_{\text{PAT}}/dV_{\text{NW}}$ as a function of V_{NW} and V_{DET} for device NW3 at gate setting A (panels (a),(b)) and setting B (panels (d), (e)) at zero and finite magnetic field, respectively. A linear fit and fits with a fixed slope $e^* = 2e$ and $e^* = e$ are shown as an orange line, a dashed green line and a dashed red line, respectively. Two normalized and smoothed horizontal linecuts are also presented, where arrows point at the position of the extracted peaks. The evolution of $e^*(B)$ and $\Delta_{\text{DET}}(B)$ is shown in panels (c) and (f). A transition from 2π - to 4π -periodic Josephson radiation is observed for gate setting A, but the radiation remains 2π -periodic for setting B. The gate voltage values are shown in table S2 of the SI.

We observe a single Josephson radiation frequency in the 4π -periodic regime, which is consistent with the supercurrent being predominantly carried by a single transmitting mode. While we were not able to reliably extract the transparency and the number of modes in our

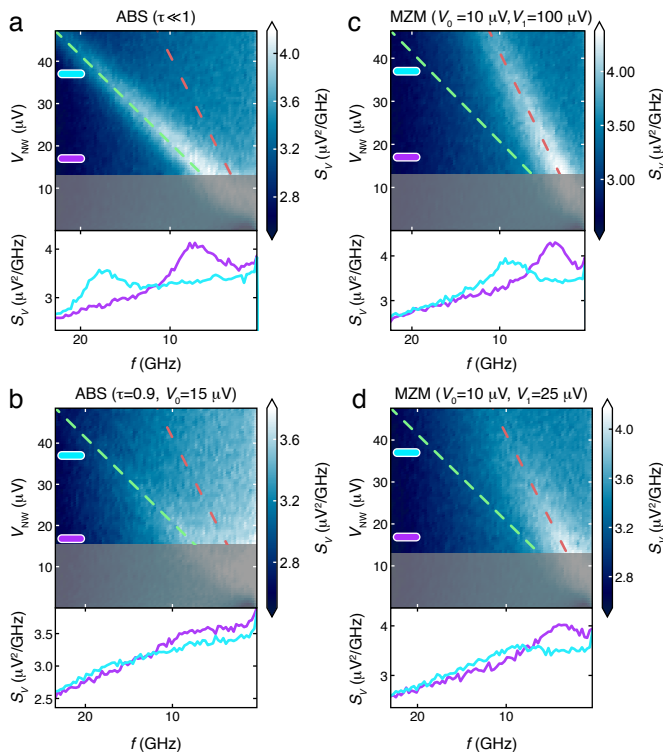


FIG. 4. The calculated radiation spectrum. The voltage spectral density $S_V(f)$ incident on the detector junction, computed by numerically solving the system of stochastic differential equations shown in Sec. 7 of the SI. Panels (a) and (b) show results for a junction in the trivial regime (small transmission and large transmission, respectively), while panels (c) and (d) show the emission spectrum in the topological regime. V_0 and V_1 are voltage scales for Landau-Zener tunneling between branches of the junction bound state and for tunneling to the quasiparticle continuum, respectively, see text. Circuit parameters are set as $r_{\text{NW}} = 2.4 \text{ k}\Omega$, $R_{\text{NW}} = 50 \text{ k}\Omega$, $R = 0.5 \text{ k}\Omega$, $C = 10 \text{ fF}$, $C_C = 400 \text{ fF}$, and $I_{\text{NW}}^0 = 8 \text{ nA}$. The noise temperature is $T = 150 \text{ mK}$ and the quasiparticle poisoning rate is $\Gamma_q = 100 \text{ MHz}$. As in Fig. 2, the dashed green and red lines show the frequency of the Josephson radiation corresponding to $e^* = 2e$ and $e^* = e$, respectively. The estimated phase diffusion region is shaded in gray.

devices, the single mode regime was observed earlier in similar InAs nanowires [46–48]. We also note that an upper bound on the channel transmission of $\tau = G_N/G_0$ can be determined from the normal state conductance $G_N < G_0$ which is shown in Fig. 2 and Fig. 3 for each device.

Next, we numerically evaluate the expected voltage spectral density seen by the detector junction in various regimes. We use the quasichlassical resistively and capacitively shunted junction (RCSJ) model coupled to a stochastic differential equation describing the occupation of the single pair of Andreev levels in the NW junction. The equivalent circuit of the device in the microwave do-

main is shown in Fig. 1b, where each element is experimentally characterized [29] (see Sec. 7 in the SI). Note that we neglect the load of the detector on the circuit, which is justified by its negligible subgap conductance compared to that of all other elements in the circuit.

Our model of the nanowire junction considers Landau-Zener (LZ) tunneling between branches of the energy-phase dispersion shown in Fig. 1a, as well as tunneling to the continuum, and stochastic quasiparticle poisoning events [33]. The probability of LZ tunneling is determined by the voltage drop V_{NW} according to the $P_{\text{LZ}} = \exp(-V_0/V_{\text{NW}})$, where $eV_0 = 4\pi\epsilon_M^2/(\Delta_{\text{NW}}\sqrt{\tau})$ is the characteristic voltage above which $P_{\text{LZ}} \sim 1$. In this limit, 4π -periodicity is observed despite the gap ϵ_M caused by finite-size effects [23]. Similarly, LZ tunneling to the continuum close to $\varphi = 2\pi$ defines a voltage scale $eV_1 = 2\pi\Delta_{\text{NW}}(1 - \sqrt{\tau})^2/\sqrt{\tau}$, above which 2π -periodicity is restored [33]. We note that a trivial Andreev bound state in the short junction limit can be modeled similarly with $eV_0 = \pi\Delta_{\text{NW}}(1 - \tau)$ and $eV_1 = 0$.

Fig. 4 shows representative plots obtained by numerically evaluating $S_V(f, V_{\text{NW}})$ (see Sec. 7.5 of the SI), which determines the photon-assisted tunneling current by Eq. (2). We observe that the numerical results agree well with the characteristic features of the experimental data. We find that the circuit equations allow for a phase diffusion regime at low V_{NW} values [44], where $e^*V_{\text{NW}} < hf$, because the junction spends part of the time in the steady supercurrent state where the voltage drop is zero. The calculations also reproduce the absence of higher harmonics in the radiation spectrum, attributed to the low transmission of the junction and overdamped nature of the microwave environment [41]. This confirms our expectation of the suppression of multiphoton processes due to a low quality factor, justifying the usage of the semiclassical junction model.

A key result of these simulations is that, with the circuit parameters taking values representative of those in the experiment, the radiation frequency always reflects the internal dynamics of the nanowire Josephson junction both in the 2π -periodic (Fig. 4a and b) and in the 4π -periodic emission regime (Fig. 4c and d). Finally, we note that our results are consistent with $V_0 \lesssim 15 \mu\text{eV}$ translating to an avoided crossing $\epsilon_M \lesssim 10 \mu\text{V}$. Using the exponential cutoff in Ref. [23], this suggests that our devices have a continuous topological region longer than $0.8 \mu\text{m}$ on each side of the nanowire junction.

In conclusion, we observed the 4π -periodic Josephson effect in multiple InAs nanowires above a threshold magnetic field in a range of $175 - 300 \text{ mT}$. This effect, which can be suppressed by tuning the gate voltages, is consistent with the expected signatures of a topological phase transition. By observing the periodicity of the Josephson effect using an *on-chip* microwave detector, we investigated this system whilst preserving its charge parity, in line with the requirements for prospective topological

quantum computers. This experimental technique may also prove instrumental in identifying more exotic non-Abelian anyon states [49, 50], due to its proven sensitivity to the periodicity of the Josephson effect, directly measuring the charge fractionalization of the anyon state [51, 52].

DATA AVAILABILITY

The datasets generated and analysed during this study are available at the 4TU.ResearchData repository, DOI: 10.4121/uuid:1f936840-5bc2-40ca-8c32-1797c12cacb1 (Ref. [53]).

ACKNOWLEDGEMENTS

The authors acknowledge O. Benningshof, J. Mensingh, M. Quintero-Pérez and R. Schouten for technical assistance. This work has been supported by the Dutch Organization for Fundamental Research on Matter (FOM), Microsoft Corporation Station Q, the Danish National Research Foundation and a Synergy Grant of the European Research Council. A. G. acknowledges the support of the Netherlands Organization for Scientific Research (NWO) by a Veni grant.

AUTHOR CONTRIBUTIONS

D. L., D. B., D. J. v. W. and A. P. fabricated the samples and performed the experiments. P. K. and J. N. contributed to the nanowire growth. L. P. K. and A. G. designed and supervised the experiments. C. M., D. P. and C. N. developed the theoretical model of the devices. D. L., D. B., D. J. v. W., R. J. J. v. G., L. P. K. and A. G. analyzed the data. The manuscript has been prepared with contributions from all the authors.

* These authors contributed equally to this work.

† To whom correspondence should be addressed; E-mail: a.geresdi@tudelft.nl

- [1] Kitaev, A. Y. Unpaired Majorana fermions in quantum wires. *Physics-Uspekhi* **44**, 131 (2001).
- [2] Nayak, C., Simon, S. H., Stern, A., Freedman, M. & Das Sarma, S. Non-abelian anyons and topological quantum computation. *Rev. Mod. Phys.* **80**, 1083–1159 (2008).
- [3] Hyart, T. *et al.* Flux-controlled quantum computation with Majorana fermions. *Phys. Rev. B* **88**, 035121 (2013).
- [4] Aasen, D. *et al.* Milestones toward Majorana-based quantum computing. *Phys. Rev. X* **6**, 031016 (2016).

- [5] Karzig, T. *et al.* Scalable designs for quasiparticle-poisoning-protected topological quantum computation with Majorana zero modes. *Phys. Rev. B* **95**, 235305 (2017).
- [6] Mourik, V. *et al.* Signatures of Majorana fermions in hybrid superconductor-semiconductor nanowire devices. *Science* **336**, 1003–1007 (2012).
- [7] Das, A. *et al.* Zero-bias peaks and splitting in an Al-InAs nanowire topological superconductor as a signature of Majorana fermions. *Nature Physics* **8**, 887–895 (2012).
- [8] Deng, M. T. *et al.* Anomalous zero-bias conductance peak in a Nb–InSb nanowire–Nb hybrid device. *Nano Letters* **12**, 6414–6419 (2012).
- [9] Churchill, H. O. H. *et al.* Superconductor-nanowire devices from tunneling to the multichannel regime: Zero-bias oscillations and magnetoconductance crossover. *Phys. Rev. B* **87**, 241401 (2013).
- [10] Deng, M. *et al.* Majorana bound state in a coupled quantum-dot hybrid-nanowire system. *Science* **354**, 1557–1562 (2016).
- [11] Zhang, H. *et al.* Quantized Majorana conductance. *Accepted in Nature*, *arXiv:1710.10701* (2017).
- [12] Rainis, D. & Loss, D. Majorana qubit decoherence by quasiparticle poisoning. *Phys. Rev. B* **85**, 174533 (2012).
- [13] Josephson, B. D. Possible new effects in superconductive tunnelling. *Phys. Lett.* **1**, 251–253 (1962).
- [14] Liu, J., Potter, A. C., Law, K. T. & Lee, P. A. Zero-bias peaks in the tunneling conductance of spin-orbit-coupled superconducting wires with and without Majorana end-states. *Phys. Rev. Lett.* **109**, 267002 (2012).
- [15] Pikulin, D. I., Dahlhaus, J. P., Wimmer, M., Schomerus, H. & Beenakker, C. W. J. A zero-voltage conductance peak from weak antilocalization in a Majorana nanowire. *New Journal of Physics* **14**, 125011 (2012).
- [16] Kells, G., Meidan, D. & Brouwer, P. Low-energy sub-gap states in multichannel p-wave superconducting wires. *Phys. Rev. B* **85**, 060507 (2012).
- [17] Lee, E. J. *et al.* Spin-resolved Andreev levels and parity crossings in hybrid superconductor-semiconductor nanostructures. *Nature Nanotechnology* **9**, 79–84 (2014).
- [18] Liu, C.-X., Sau, J. D., Stanescu, T. D. & Das Sarma, S. Andreev bound states versus Majorana bound states in quantum dot-nanowire-superconductor hybrid structures: Trivial versus topological zero-bias conductance peaks. *Phys. Rev. B* **96**, 075161 (2017).
- [19] Deblock, R., Onac, E., Gurevich, L. & Kouwenhoven, L. P. Detection of quantum noise from an electrically driven two-level system. *Science* **301**, 203 (2003).
- [20] Krogstrup, P. *et al.* Epitaxy of semiconductor-superconductor nanowires. *Nature Materials* **14**, 400–406 (2015).
- [21] Oreg, Y., Refael, G. & von Oppen, F. Helical liquids and Majorana bound states in quantum wires. *Phys. Rev. Lett.* **105**, 177002 (2010).
- [22] Lutchyn, R. M., Sau, J. D. & Sarma, S. D. Majorana fermions and a topological phase transition in semiconductor-superconductor heterostructures. *Phys. Rev. Lett.* **105**, 077001 (2010).
- [23] Albrecht, S. *et al.* Exponential protection of zero modes in Majorana islands. *Nature* **531**, 206–209 (2016).
- [24] Hofheinz, M. *et al.* Bright side of the Coulomb blockade. *Phys. Rev. Lett.* **106**, 217005 (2011).
- [25] Giaever, I. Detection of the ac Josephson effect. *Phys. Rev. Lett.* **14**, 904 (1965).

- [26] Grimes, C., Richards, P. & Shapiro, S. Far infrared response of point-contact Josephson junctions. *Phys. Rev. Lett.* **17**, 431 (1966).
- [27] Cleuziou, J.-P. *et al.* Gate-tuned high frequency response of carbon nanotube Josephson junctions. *Phys. Rev. Lett.* **99**, 117001 (2007).
- [28] Doh, Y.-J. *et al.* Tunable supercurrent through semiconductor nanowires. *Science* **309**, 272–275 (2005).
- [29] van Woerkom, D. J. *et al.* Josephson radiation and shot noise of a semiconductor nanowire junction. *Phys. Rev. B* **96**, 094508 (2017).
- [30] Chen, J., Wenger, L., McEwan, C. & Logothetis, E. Observation of the reverse ac Josephson effect in Y-Ba-Cu-O at 240 K. *Phys. Rev. Lett.* **58**, 1972 (1987).
- [31] Fu, L. & Kane, C. L. Josephson current and noise at a superconductor/quantum-spin-Hall-insulator/superconductor junction. *Phys. Rev. B* **79**, 161408 (2009).
- [32] San-Jose, P., Prada, E. & Aguado, R. ac Josephson effect in finite-length nanowire junctions with Majorana modes. *Phys. Rev. Lett.* **108**, 257001 (2012).
- [33] Pikulin, D. I. & Nazarov, Y. V. Phenomenology and dynamics of a Majorana Josephson junction. *Phys. Rev. B* **86**, 140504 (2012).
- [34] Houzet, M., Meyer, J. S., Badiane, D. M. & Glazman, L. I. Dynamics of Majorana states in a topological Josephson junction. *Phys. Rev. Lett.* **111**, 046401 (2013).
- [35] Higginbotham, A. *et al.* Parity lifetime of bound states in a proximitized semiconductor nanowire. *Nature Physics* **11**, 1017–1021 (2015).
- [36] Albrecht, S. M. *et al.* Transport signatures of quasiparticle poisoning in a Majorana island. *Phys. Rev. Lett.* **118**, 137701 (2017).
- [37] Rokhinson, L. P., Liu, X. & Furdyna, J. K. The fractional a.c. Josephson effect in a semiconductor-superconductor nanowire as a signature of Majorana particles. *Nature Physics* **8**, 795–799 (2012).
- [38] Deacon, R. S. *et al.* Josephson radiation from gapless Andreev bound states in HgTe-based topological junctions. *Phys. Rev. X* **7**, 021011 (2017).
- [39] Tucker, J. R. & Feldman, M. J. Quantum detection at millimeter wavelengths. *Reviews of Modern Physics* **57**, 1055 (1985).
- [40] Bretheau, L., Girit, Ç. Ö., Pothier, H., Esteve, D. & Urbina, C. Exciting Andreev pairs in a superconducting atomic contact. *Nature* **499**, 312–315 (2013).
- [41] Cawthorne, A. B., Whan, C. B. & Lobb, C. J. Complex dynamics of resistively and inductively shunted Josephson junctions. *Journal of Applied Physics* **84**, 1126–1132 (1998).
- [42] Scheer, E., Joyez, P., Esteve, D., Urbina, C. & Devoret, M. H. Conduction channel transmissions of atomic-size Aluminum contacts. *Phys. Rev. Lett.* **78**, 3535 (1997).
- [43] Dolan, G. Offset masks for lift-off photoprocessing. *Applied Physics Letters* **31**, 337 (1977).
- [44] Ivanchenko, Y. M. & Zil’berman, L. A. The Josephson effect in small tunnel contacts. *Sov. Phys. JETP* **28**, 1272 (1969).
- [45] Efron, B. & Tibshirani, R. Bootstrap methods for standard errors, confidence intervals, and other measures of statistical accuracy. *Statistical Science* **1**, 54–75 (1986).
- [46] van Woerkom, D. J. *et al.* Microwave spectroscopy of spinful Andreev bound states in ballistic semiconductor Josephson junctions. *Nature Physics* **13**, 876–881 (2017).
- [47] Spanton, E. M. *et al.* Current-phase relations of few-mode InAs nanowire Josephson junctions. *Nature Physics* **13**, 1177–1181 (2017).
- [48] Goffman, M. F. *et al.* Conduction channels of an InAs-Al nanowire Josephson weak link. *New Journal of Physics* **19**, 092002 (2017).
- [49] Lindner, N. H., Refael, G. & Stern, A. Fractionalizing Majorana fermions: Non-abelian statistics on the edges of abelian quantum Hall states. *Phys. Rev. X* **2**, 041002 (2012).
- [50] Clarke, D. J., Alicea, J. & Shtengel, K. Exotic non-Abelian anyons from conventional fractional quantum Hall states. *Nature Communications* **4**, 1348 (2013).
- [51] Zhang, F. & Kane, C. L. Time-reversal-invariant Z_4 fractional Josephson effect. *Phys. Rev. Lett.* **113**, 036401 (2014).
- [52] Laflamme, C., Budich, J., Zoller, P. & Dalmonte, M. Non-equilibrium 8π Josephson effect in atomic Kitaev wires. *Nature Communications* **7**, 12280 (2016).
- [53] Laroche, D. *et al.* Observation of the 4π -periodic Josephson effect in InAs nanowires. 4TU.ResearchData repository. [Http://dx.doi.org/10.4121/uuid:1f936840-5bc2-40ca-8c32-1797c12cacb1](http://dx.doi.org/10.4121/uuid:1f936840-5bc2-40ca-8c32-1797c12cacb1).